J Mater Sci (2012) 47:199–207
DOI 10.1007/s10853-011-5787-y

Metallurgical and mechanical characterization of electron beam welded DP600 steel joints

P. Ferro · A. Tiziani

Received: 25 March 2011 / Accepted: 11 July 2011 / Published online: 20 August 2011

Abstract Several new commercial advanced high-strength steels exhibit high strength and enhanced formability. These materials have the potential to affect cost and weight saving while improving performance. However, welding, by modifying the microstructure of the steel, has in general a detrimental effect on the mechanical properties of structural components. If high power density technologies are used, the result is that the mechanical properties of such kind of joints can be improved. This article presents a metallurgical and mechanical characterization of electron beam welded joints in advanced high-strength steel DP600. The experimental analysis was supported by a thermal numerical model obtained through the Sysweld® code. Results show that mechanical properties of the electron beam welded joints are comparable with those of parent metal both in terms of static strength and ductility.

Introduction

Advanced high-strength steels (AHSS) were developed in order to meet the increasing requirements of weigh reduction in many engineering applications. Their final micro-structure is usually a composite of relatively soft ferrite matrix with strengthening phases (martensite, bainite and precipitates). Thinner sheets can also be used in automobile bodies since AHSS have better impact energy absorbing capacity and resistance to plastic deformation with respect to conventional ferritic low-carbon sheet steels [1–4]. In general, weight reduction involves less material purchased, less production energy, less CO_2 emissions, less inertial loads and, finally, less environmental harm. The increased formability of these steels allows for greater part complexity, which leads to fewer individual parts (cost savings) and more manufacturing flexibility.

AHSS are typically produced by nontraditional thermal cycles and contain microstructural components whose mechanical properties can be altered by exposure to elevated temperatures. This temperature sensitivity could alter the mechanical behaviour of AHSS after welding. Thus, the weldability is one of the main technological properties, which have to be investigated in order to correctly use such materials in structural and mechanical applications.

The fusion welding processes have historically been, and they are today, commonly used in manufacturing of automotive structures. Recently, the increased use of AHSS in automotive design posed a desire to evaluate the application of fusion welding processes relative to the joining of AHSS [5–9].

Among the welding technologies, high power density processes has received attention because of high-production rate and good metallurgical properties of the joined metals: reduced extension of heat affected zone (HAZ), fusion zone (FZ) and low deformations [10, 11]. Despite this, investigations on laser and electron beam AHSS welded joints are still lacking in literature.

In their work, Rizzi et al. [12] have studied the effect of laser welding on the microstructure of three AHSS: transformation induced plasticity steel (TRIP), dual-phase steel (DP) and martensitic steel. The FZ microstructure was constituted by martensite and a continuous change in microstructure was observed along the HAZ. Due to the solidification undercooling the formation of austenite as primary phase was expected. Another interesting study was carried out by Kang et al. [13] who investigated the

---

P. Ferro (✉) · A. Tiziani
Department of Management and Engineering, University of Padova, Stradella S. Nicola, 3, 36100 Vicenza, Italy
e-mail: ferro@gest.unipd.it

characteristics of Nd:YAG laser welded 600 MPa grade TRIP and DP steels in relation to hardness, microstructures, mechanical properties and formability. In both steels the hardness of the weld zone was increased compared with the base metal, even though the region showing the maximum hardness was different. In particular, the maximum hardness for DP was obtained at HAZ near the weld metal. Martensite and bainite were observed in the weld metal of TRIP while upper bainite, acicular ferrite and martensite were shown in the weld metal of DP. In a tensile test perpendicular to the weld axis, all specimens were broken at the base metal and the tensile strength and yield strength were higher than those of the raw material but the elongation was lower. Finally, formability was determined to be approximately 80% when compared with the raw material.

Xia et al. [14] investigated the effects of heat input on HAZ softening of three dual-phase alloys with ultimate tensile strengths ranging from 450 to 980 MPa. It was found that HAZ softening was a function of both martensite content and heat input. In particular, maximum HAZ softening was proportional to the martensite content, and the heat input controlled the completion of softening. A more recent experimental work on laser welded DP steel joints was carried out by Farabi et al. [15]. They evaluated the microstructural change after laser welding and its effect on the tensile and fatigue properties. According to the previous works, a ductility decrease and yield strength increase after welding was found. Due to the strain ageing effect, the welded DP600 steel joints were observed to exhibit slightly yield phenomena, compared to the base metal. Although the fatigue limit of the welded joints was slightly lower than that of the base metal, the fatigue life at the higher level of stress amplitudes was almost the same (within the experimental scatter between the base metal and welded joints) despite the presence of the soft zone. Tensile fracture and fatigue failure at higher stress amplitude occurred at the outer HAZ. In a previous work, Tiziani et al. [16] investigated the effects of different welding technologies on metallurgical and mechanical properties of DP600 steel joints. In that work, they found a FZ microstructure constituted by a mixture of acicular, bainitic and allotriomorphic ferrite; a soft zone was detected which extension increased with the increase of the heat input. As a consequence, all samples failed in the outer HAZ where the minimum hardness was detected. However, electron beam welded joints showed better mechanical properties compared to the gas tungsten and plasma arc welded samples.

In this study, electron beam DP600 steel welded joints are analysed both in terms of metallurgical and mechanical properties. A thermal numerical simulation of the process is also used to correlate the thermal history with the observed microstructures. The electron beam DP600 steel welded joints showed good mechanical properties which are very close to those of the parent metal.

Material and experimental procedure

Material

The DP600 steel having a thickness of 2 mm was selected in this study. The chemical composition of the base metal is shown in Table 1.

Electron beam welding (EBW)

Electron beam welding was conducted at a welding speed of 9 mm/s and a beam power of 1125 W in full penetration bead on a plate mode. Details about process parameters are collected in Table 2.

Metallography and microhardness testing

After welding, transverse cross sections of the welds were cut and examined by light optical microscopy, after metallographic preparation and etching (2% Nital

Table 2 EBW process parameters

	Value
Parameter	
Accelerating voltage	150 kV
Vacuum chamber	≤0.0008 mbar
Vacuum gun	≤0.000004 mbar
Beam current	7.5 mA
Beam focus	367 mA (surface)
Weld speed	9 mm/s
Beam slope up	0.1 mm
Beam slope down	2 mm
Function generation	
Frequency	9999 Hz
Amplitude *X*	14
Amplitude *Y*	14
Pattern	5 (circular)

Table 1 Chemical composition (wt%) of the DP600 steel selected in this study

C	Mn	Si	S	P	Cr	Ni	Mo	Al	Co	Nb	V	Ti	N	W	Cu
0.081	1.69	0.199	<0.0007	0.0165	0.455	0.047	0.001	0.0369	0.0146	0.003	0.020	0.0025	0.012	0.008	0.005

Fig. 1 Geometry of tensile test specimens used in the present study (dimensions are in mm)

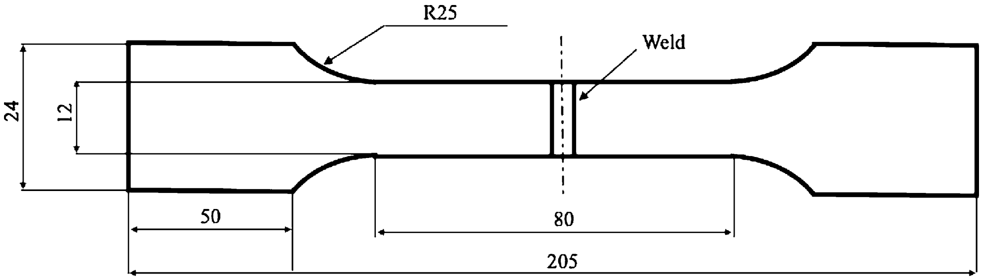

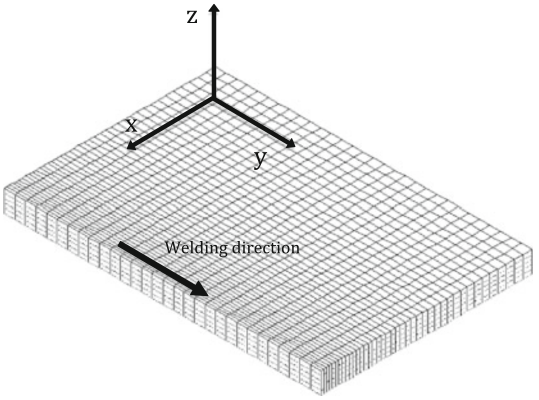

Fig. 2 Mesh of the 3D model

solution). An image analysis system (LEICA QWIN), interfaced with the light microscope, was used to observe the microstructural change across the welds and to evaluate the volume fraction of ferrite and martensite in BM with an average value of four measurements at 500×.

Vickers microhardness tests were performed on the etched samples. A load of 100 g and a dwell time of 15 s were used during testing. The centre point of the fusion zone was determined by carefully observing the weld geometry under an optical microscope and all the indentations were adequately spaced to avoid potential effect of strain fields caused by adjacent indentations.

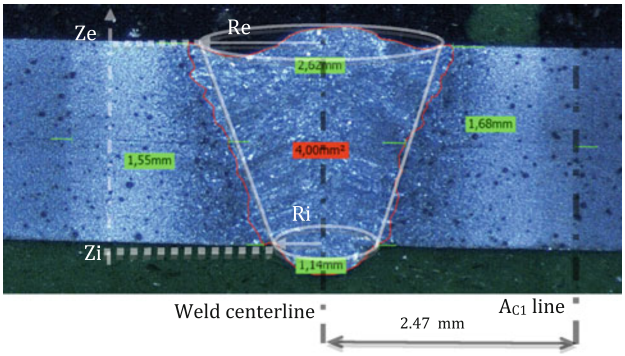

Fig. 3 Cross section of a DP600 electron beam weld with speed of 9 mm s^{-1} and geometrical parameter of the conical heat source

Tensile tests

Tensile tests were performed on base material and welded specimens in order to investigate the mechanical properties of the joints. Welded samples were machined perpendicular to the welding direction, the geometry of tensile test samples is shown in Fig. 1, in accordance with UNI EN 895 Standards. Tensile tests were performed at room temperature using a fully computerized universal tensile testing machine. Four welded samples, taken from the same joint, were tested.

Thermal numerical model

In order to gain a reliable description of the thermal field induced by EBW, a numerical model was developed which takes into account heat losses by convention/radiation and the variation of the thermal material properties with the temperature. A detailed description of the material properties used can be found in Ref. [17]. In this case, 8950 isoparametric elements were used to model the geometry and the symmetry was also used to simplify the computation (Fig. 2). Finally, due to the high thermal gradients, a dense mesh was used in the area along the weld line. The model was developed by means of the numerical code SYSWELD® 2010.

Modelling of the heat source

A three-dimensional conical heat source was used which takes into consideration the heat intensity distribution along the thickness of the metal. At any plane perpendicular to z-axis, the heat intensity is distributed in a Gaussian form and may be written as

$$q(r,z) = q_0 \exp\left(-\frac{r^2}{r_0^2}\right) \tag{1}$$

where q_0 is the maximum value of heat intensity, r_0 is the distribution parameter and r is the radial coordinate from the source center.

As shown in Fig. 3, the height of the conical heat source is $H = Z_e - Z_i$, the z-coordinates of the top and bottom

Table 3 Values of the source parameters used in Eq. 2

q_0 (W/mm^3)	R_i (mm)	R_e (mm)	z_i (mm)	z_e (mm)
360	0.2	0.86	−0.17	2.2

surfaces are Z_e and Z_i, respectively, and the radii at the top and bottom are R_e and R_i, respectively. The distribution parameter r_0 is linearly decreased from the top to the bottom surfaces of the conic region, and it can be expressed as

$$r_0(z) = R_e - \frac{(R_e - R_i)(Z_e - z)}{(Z_e - Z_i)} \qquad (2)$$

The unknown source parameters in Eqs. 1 and 2 (Z_i, Z_e, R_i, R_e and q_0) have been calibrated by using the phenomenological approach described in a previous work [18]. Table 3 summarises the values used for the simulation while Fig. 4 shows a comparison between experimental and numerical results.

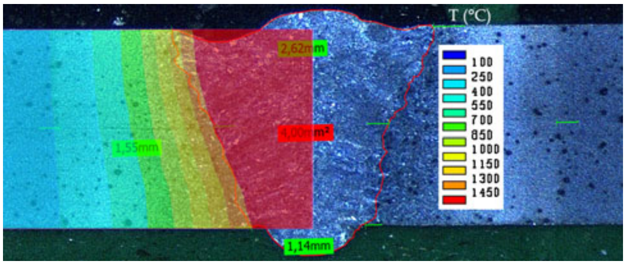

Fig. 4 Comparison between experimental and numerical FZ shape and dimensions (solidus temperature, 1450 °C)

Results and discussion

Microstructural evolution

Figure 5 shows the microstructural evolution of electron beam DP600 steel welded joints starting from the weld centreline. The base metal (Fig. 5h) consists of about 18% martensite in a matrix of polygonal (or equiaxed) ferrite (PF) while the FZ and the HAZ consist of a prevalence of rapidly solidified structures (RSS) with some islands of grain

Fig. 5 Micrographs of electron beam welded DP600 at different distances from the weld centreline (*M* martensite, *UB* upper bainite, *GF* grain boundary ferrite, *AF* acicular ferrite)

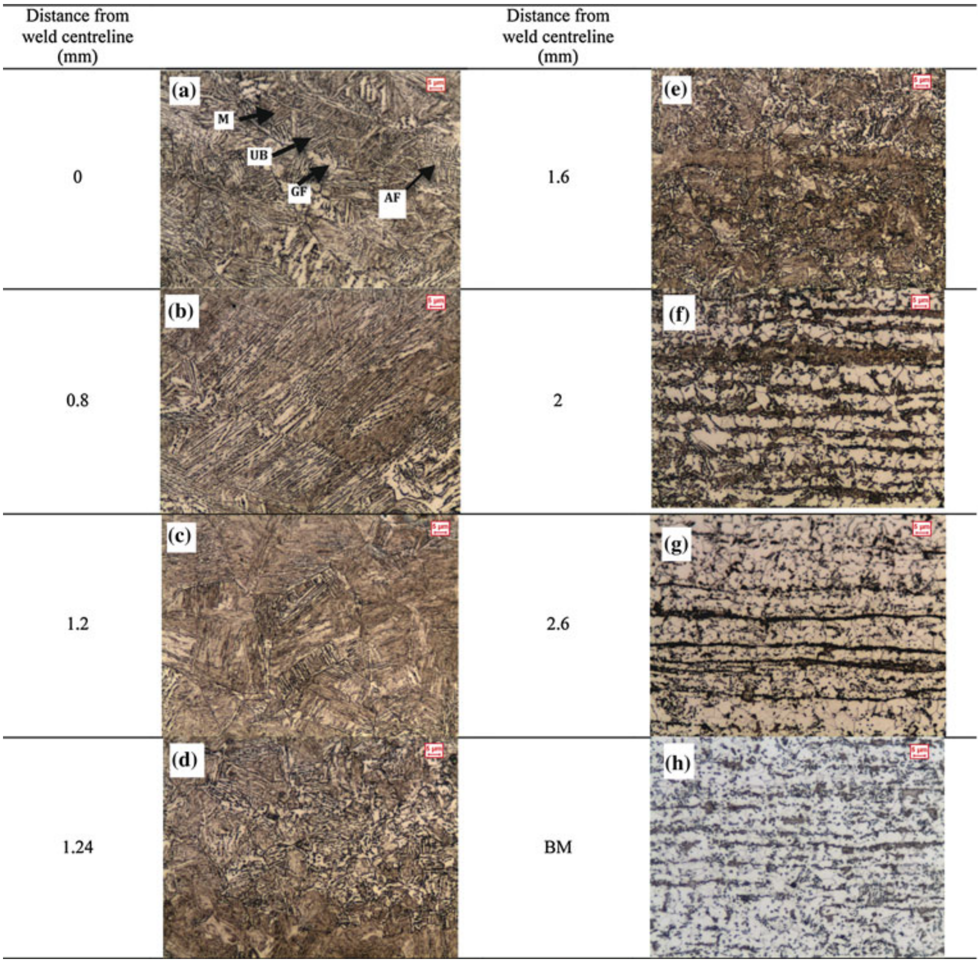

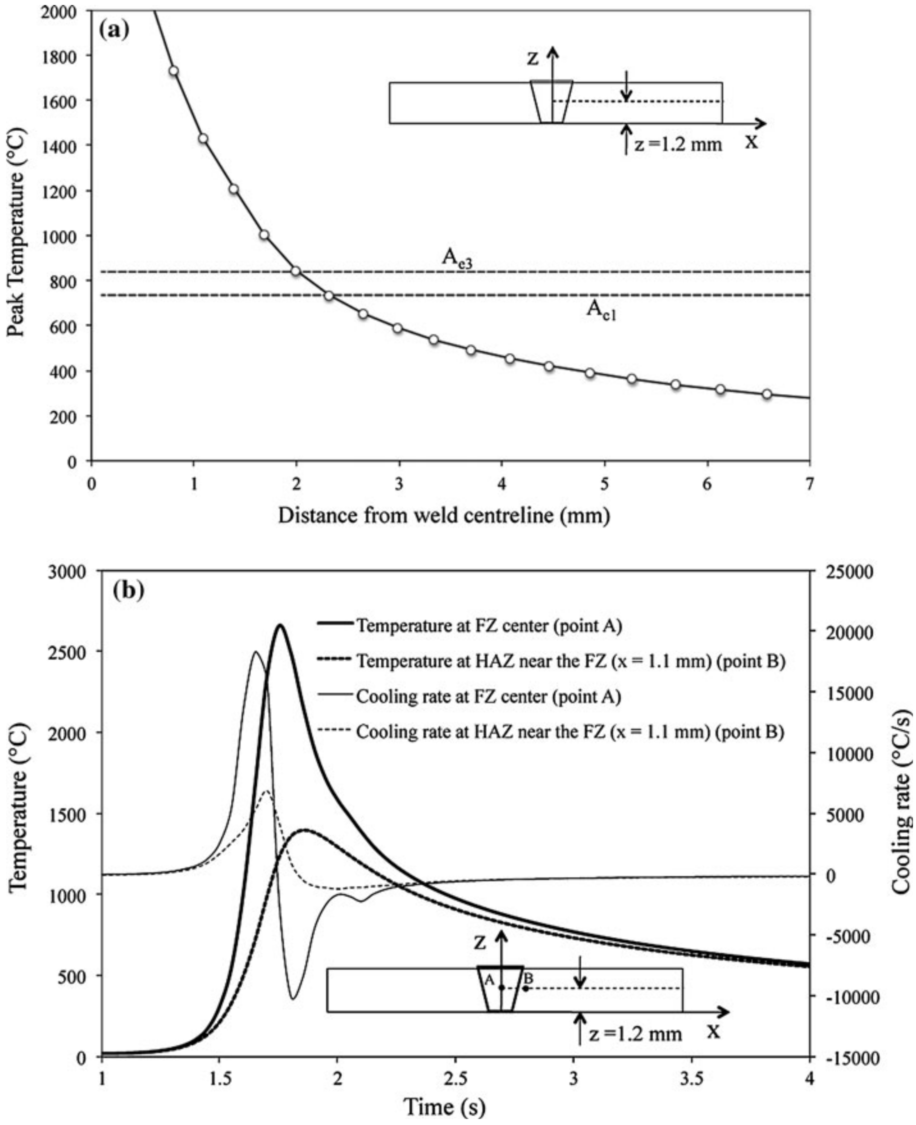

Fig. 6 **a** Calculated peak temperatures at difference distance from weld centreline; **b** temperature and cooling rate at FZ center and HAZ near the FZ

boundary (or allotriomorphic) ferrite (GF). A greater percentage of lath martensite is observed in HAZ near the weld metal (WM) (Fig. 5c) compared to the fusion zone (Fig. 5a, b). At a distance of 1.24 mm from the weld centreline (Fig. 5d), islands of equiaxed ferrite appear and, starting from 2 mm, the amount of polygonal ferrite significantly increases to the detriment of martensite (Fig. 5f, g).

In order to couple the thermal and metallurgical evolution, information about Ae_3-temperature is necessary. This temperature can be readily obtained from thermodynamic calculations, even for multicomponent systems. Alternatively, the empirical relationships quoted by Leslie [19] can be used. A value of Ae_3 equal to 840 °C was found. Furthermore, the Ac_1-temperature was estimated by using Yurioka's relation [20] to be 735 °C. Figure 6a shows the calculated peak temperature reached in the middle cross section of the plates as a function of the distance from the weld centreline. A good correlation between the experimental and calculated distance of the Ac_1 isotherm from the weld centreline was found (Figs. 3, 6a). Plate martensite was found in the region where the peak temperatures approach the Ac_1 value (Figs. 5f, g, 7a); as a matter of fact, the increasing amount of polygonal ferrite in this region increases the carbon content in austenite and thus its hardenability.

A banded microstructure was shown in this zone and in BM (Fig. 7). It is due both to the manganese content and the alloy production by casting under conditions which do not correspond to the equilibrium. There are as a result, manganese-enriched regions between the dendrites. The following solid-state processing which involves rolling-deformation is then expected to smear these enriched regions along the rolling direction, thus building into the steel bands of Mn-enriched and Mn-depleted regions. When the austenite is cooled, ferrite first forms in the

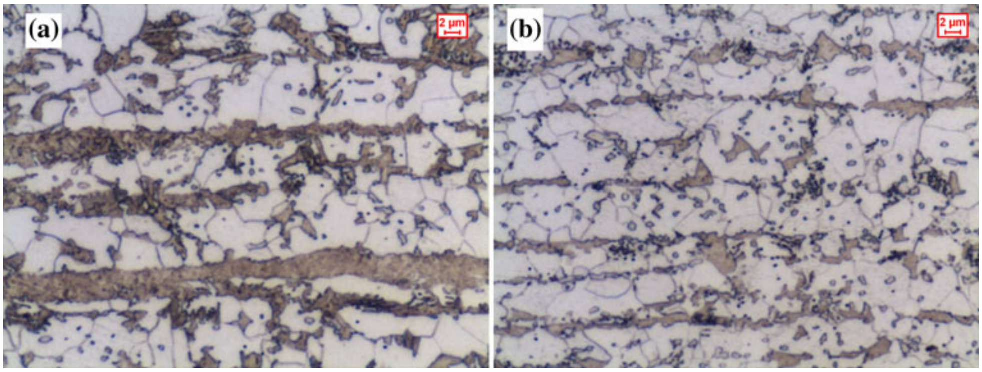

Fig. 7 **a** Micrograph of HAZ at 2 mm from the weld centreline; **b** micrograph of BM

Mn-depleted regions. Ferrite has a very low solubility for carbon which partitions into the Mn-enriched regions which after further rapid cooling, transform into bands of martensite.

The presence of bainite, islands of PF and acicular ferrite (AF) in FZ (Fig. 5a) can not be explained by simply considering the cooling rate in that zone because it was found to be higher than that calculated at HAZ, near the weld bead where the martensitic structure prevails (Fig. 6b). Different positions of the "*C*" curves that characterize the austenite transformation in FZ and HAZ are thus supposed. In FZ, during solidification, the cooling rate is sufficiently high to cause considerable chemical segregation. The austenite, when it begins to transform, is therefore far from homogeneous, and this in turn influences its transformation kinetics. Gretoft et al. [21] took this into account by calculating the liquid/delta-ferrite partitioning coefficients of substitutional alloying elements in low ally steels, and hence obtaining the composition of the solute-depleted regions of a weld. A separate isothermal transformation diagram was then calculated for the solute-depleted regions, and since austenite transforms more rapidly in these regions, it was used to calculate T_h (the temperature at which the transformation from austenite to ferrite first occurs), which turned out to be higher than that expected for a homogeneous alloy. This also means that the volume fraction of allotriomorphic ferrite obtained is higher for a heterogeneous weld.

About the presence of PF in HAZ near the FZ, assuming that ferrite nucleation occurs preferentially at the austenite grain faces, the following expression for time–temperature transformation curve can be written [22]:

$$\tau = \tau_p \left(\frac{D_\gamma}{D_\gamma^*}\right) \exp\left[\frac{A_0}{R}\left(\frac{T_{eq}^2}{T\left(T_{eq}-T\right)^2} - \frac{T_{eq}^{*2}}{T_p\left(T_{eq}^*-T_p\right)^2}\right) + \frac{Q_d}{R}\left(\frac{1}{T}-\frac{1}{T_p}\right)\right] \quad (3)$$

where τ is the time taken to precipitate a small fraction ($\sim$2%) of ferrite, T is the temperature, Q_d is the activation energy for diffusion of carbon in austenite, T_{eq} is the Ae_3 temperature of the steel, R is the gas constant, A_0 is a constant, D_γ/D_γ* is the inverse grain size ratio where D_γ and D_γ* refer to the austenite grain size in the actual and reference material, respectively; data about the reference material (Nb-microalloyed steel) is reported in Table 4 [22].

According to the peak temperature and heat input, D_γ can be calculated by means of grain growth diagrams reported in literature [22]. By using Eq. 3 and Fig. 6a, the conditions for ferrite formation at two different positions (within the HAZ) corresponding to a peak temperature T_p of 1431 and 1206 °C, respectively were found. Figure 8 shows the *C* curves in relation to the two analysed positions in HAZ (point A and B in Fig. 8). By using the corresponding calculated cooling curves (Fig. 8) and the additivity rule [22], it is possible to estimate the volume fraction of ferrite which forms at each point [22]. More generally, Fig. 8 shows a strong effect of austenite grain size on the HAZ transformation kinetics. This may explain the microstructures observed in Fig. 5c–e.

Microhardness and tensile properties

Figure 9 shows the micro-indentation hardness profile of electron beam welded DP600. Significantly high hardness values were observed in the HAZ near the FZ where the microstructure is mainly constituted by lath martensite. To confirm such results, a water quenching heat treatment was

Table 4 Input data used to construct *C* curve for PF in reference steel [22]

Parameter	T_r (K)	τ_r (s)	T_{eq}^* (K)	A_0 (J mol^{-1})	Q_d (kJ mol^{-1})	D_γ^*(μm)
value	823	0.6	1108	700	135	10

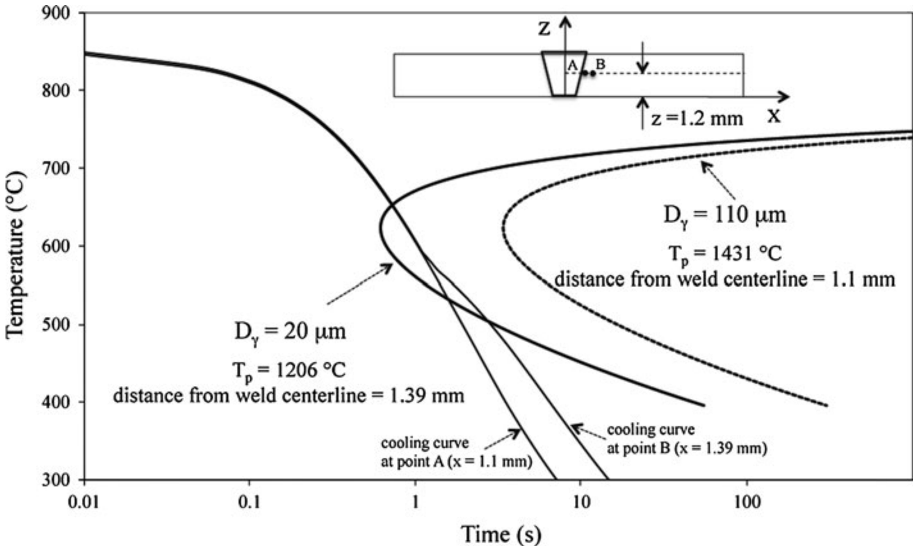

Fig. 8 Effect of austenite grain size on the HAZ transformation kinetics in electron beam welded DP600

carried out on the base metal in order to measure the hardness of martensite. Values ranging from 350 and 400 Vickers were found. The hardness of the weld metal is lower than that of HAZ near the weld metal due to the mixture of soft and hard phases. The variable hardness appearing in the FZ reflects the presence of such a multi-constituent microstructure. The decrease in the hardness of HAZ near the base metal results from the presence of a relatively soft ferrite which increases as the weld metal approaches the base metal.

Due to the variable microhardness profile in HAZ near the base metal and in BM, it was not possible to appreciate the soft zone referred to in literature concerning laser welding of DP600, which is attributed to the tempering of pre-existing martensite. This may be due to the following reasons: the relatively low amount of pre-existing martensite and the low heat input as described by Xia et al. [14].

Tensile properties

Figure 10 shows the engineering stress–strain curves obtained from both the base metal and the welded joints. It is of interest to note that the stress–strain curve of DP600 welded joint shows yield point phenomena while the curve of the base material is smooth. This difference is also noted in literature [14, 16] for the DP600 laser welded joints. The welded joints had higher yield strength than the base metal while the tensile strength of the welded specimens was very close to that of base metal.

The yield point phenomena, in the welded samples, are attributed to interstitial diffusion which might occur during the welding process [15]. The heating induced on the plates by welding drives the carbon (or nitrogen) atoms in iron to diffuse to a position of high energy which is just below the extra plane of atoms in edge dislocations. Thus, a large portion of the mobile dislocations becomes sessile. When a sufficiently large stress is applied, dislocation can break free from solute clusters and cause a load drop as seen in Fig. 10. Some detailed descriptions on the source of upper yield point, which was the drop of the load after onset of yielding, can be found in the literature [23–27].

It is of interest also to note that all the welded samples failed at the base metal as shown in Fig. 11. This behaviour is probably due to the absence of a detectable soft zone which is often found in dual-phase steel welded joints. As a matter of fact, as referred to literature, the failure of DP welded joints typically occurs in the soft zone [15, 16]. This results in an early appearance of necking and consequently a reduction of elongation when compared to the base metal. Even though the analysed electron beam welded joints show a reduction in the elongation, the difference with the base metal is less marked compared to the values found in literature about laser or arc welded DP600 steel joints [15, 16].

Conclusions

A metallurgical and mechanical characterization of electron beam welded DP600 steel joints was made. A numerical model was used for the prediction of the thermal history which was induced by the process and its correlation with the microstructures found in FZ and HAZ. On the basis of the experimental observations and numerical results, the following conclusions can be made:

1. A mixture of RSS with some islands of allotriomorphic ferrite was found in FZ and HAZ. In HAZ, near the weld metal, a prevalence of martensite was detected.

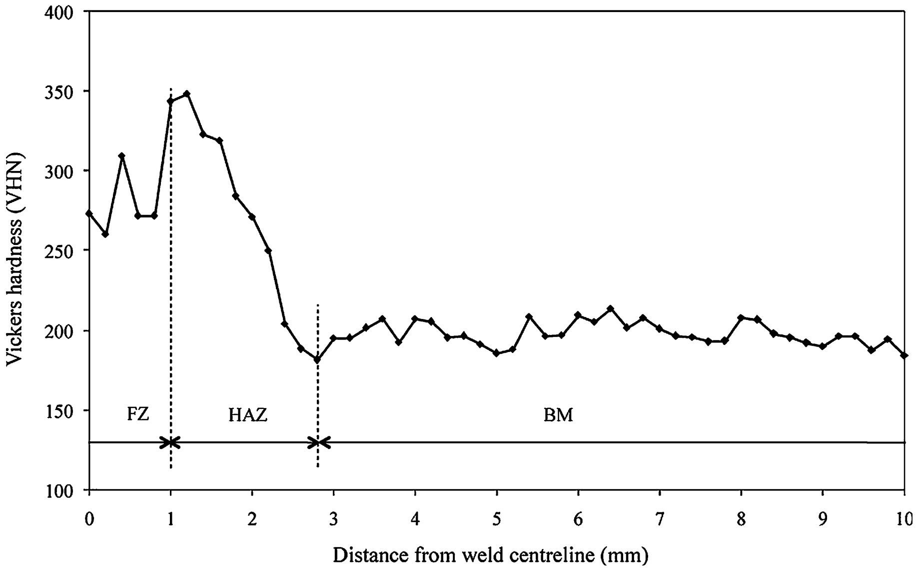

Fig. 9 Microhardness profile of the electron beam welded DP600

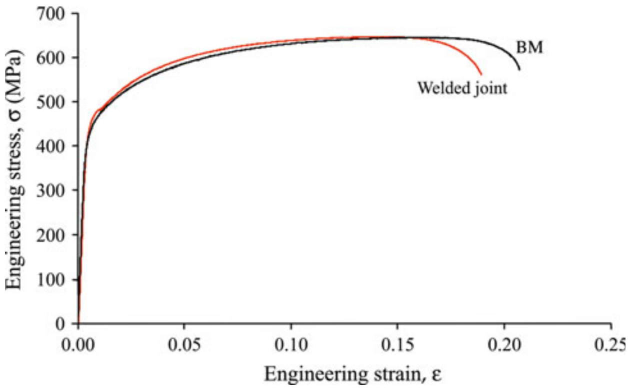

Fig. 10 Comparison between engineering stress–strain curves of the DP600 EB welded joint and base metal (cross-head speed = 2 mm/min)

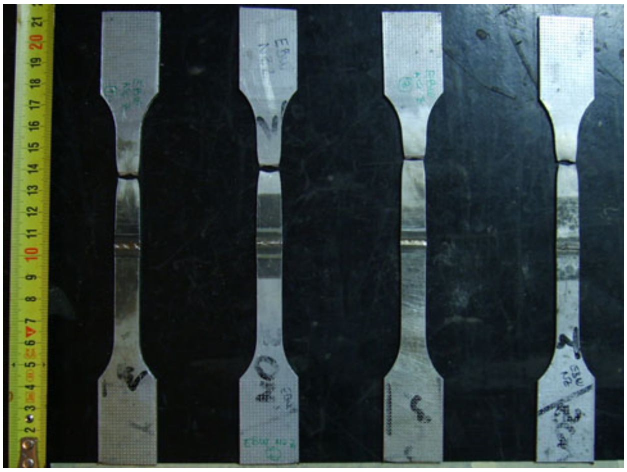

Fig. 11 Failure location of the tensile test samples of the electron beam welded DP600 steel joints

2. The presence of polygonal ferrite in HAZ was attributed to the relative low peak temperatures (compared to those found in the HAZ/BM interface) which limited the austenite grain coarsening and thus changed the position of the ferrite *C* curve.
3. Microhardness profiles accurately reflect the observed microstructure, with maximum hardness values at HAZ, near the weld bead, where the martensitic structure prevails. The approaching the base metal from the weld metal, the decrease in hardness resulted in an increase amount of soft ferrite.
4. The welded joints were seen to have a higher yield strength and exhibit slightly yield point phenomena, in comparison with the base metal. The typical softening effect in HAZ was not detected. This is probably due to the low heat input and the small fraction of pre-existing martensite. Consequently, a small difference in elongation was found between the welded joints and the parent metal and welded joints failed at BM.

References

1. Zackay VF, Parker ER, Fhhr D, Bush R (1967) Trans ASM 60:252
2. Olson GB, Cohen M (1976) Metall Trans 7A:1897
3. Chen HC, Era H, Shimizu M (1989) Metall Trans 20A:437
4. Sugimoto K, Misu M, Kobayashi M, Shirasawa H (1993) ISIJ Int 33:775
5. Ma C, Chen DL, Bhole SD, Boudreau G, Lee A, Biro E (2008) Mater Sci Eng A 485:334
6. Rossillon F, Galtier A, Robert JL, Duchet M, Lens A, Oikawa H (2008) Weld World 52:30
7. Ghosh PK, Gupta PC, Avtar R, Jha BK (1990) ISIJ Int 30:233
8. Daneshpour S, Riekehr S, Kocak M, Gerritsen CHJ (2009) Sci Technol Weld Join 14:20

9. Koganti R, Angotti S, Joaquin A, Jiang C, Karas C (2008) In: Proceedings of ASME international mechanical engineering congress and exposition, IMECE 2007, Ser. 3. American Society of Mechanical Engineers, Seattle, 11–15 November 2007
10. Larsson JK (2003) Weld Res Abroad 49:29
11. Chung-Yun K, Tae-Kyo H, Bong-Keun L, Jeong-Kil K (2007) Mater Sci Forum 539–543:3967
12. Rizzi P, Bellingeri S, Massimino F, Baldissin D, Battezzati L (2009) J Phys Conf Ser 144:012005
13. Kank C-Y, Han T-K, Lee B-K, Kim J-K (2007) Mater Sci Forum 539(543):3967
14. Xia M, Biro E, Tian Z, Norman Zhou Y (2008) ISIJ Int 48(6):809
15. Farabi N, Chen DL, Li J, Zhou Y, Dong SJ (2010) Mater Sci Eng A 527:1215
16. Tiziani A, Ferro P, Cervo R, Durante M (2011) La Metall Italiana 1:27
17. Schenk T, Richarson IM, Kraska M, Ohnimus S (2009) Comput Mater Sci 46:977
18. Ferro P, Zambon A, Bonollo F (2005) Mater Sci Eng A 392:94
19. Leslie WC (1981) The physical metallurgy of steels. McGraw-Hill, London
20. Yurioka N (2011) Weldability calculation. http://homepage3.nifty.com/yurioka/. Accessed Feb 2011
21. Gretoft B, Bhadeshia H, Svensson LE (1986) Acta Stereol 5:365
22. Grong Ø (1994) In: Bhadeshia HKDH (ed) Metallurgical modelling of welding, 2nd edn. The Institute of Materials, London
23. Hertzberg RW (1995) Deformation and fracture mechanics of engineering materials, 4th edn. Wiley, Weinheim
24. Callister WD Jr (2007) Material sciece and engineering—an introduction, 7th edn. Wiley, New York
25. Dieter GE (1988) Mechanical metallurgy, SI metric edition. McGraw-Hill Book Co, London
26. Gaur A (2011) Effect of strain ageing on welded or non-welded low carbon steel. Thesis. http://ethesis.nitrkl.ac.in/1157/1/strain_ageing.pdf. Accessed Feb 2011
27. Wilson DV, Russel B, Eshelby JD (1959) Acta Metall 7(9):628